

Magnetism and Magnetotransport in the Kagome Antiferromagnet Mn_3Ge

Gaurav Chaudhary,¹ Anton A. Burkov,^{2,3} and Olle G. Heinonen¹

¹*Materials Science Division, Argonne National Laboratory, Lemont, IL 60439, USA*

²*Department of Physics and Astronomy, University of Waterloo, Waterloo, Ontario N2L 3G1, Canada*

³*Perimeter Institute for Theoretical Physics, Waterloo, Ontario N2L 2Y5, Canada*

(Dated: February 21, 2022)

We perform classical Monte Carlo and stochastic Landau-Lifshitz-Gilbert simulations to study temperature dependent magnetism of Kagome antiferromagnet (AFM) Weyl metal Mn_3Ge and find that a long range chiral order sets in at a transition temperature well below the Néel temperature (T_N). Based on the crystalline symmetries, imposed by the chiral magnetic order, we argue for the presence of multiple iso-energetic Weyl nodes (nodes that are at same energy and with congruent Fermi surface around them) near chemical potential. Using the semi-classical Boltzmann equations, we show that the combined contribution to the net longitudinal magnetoconductance (LMC) and the planar Hall conductance (PHC) from tilted Weyl nodes can lead to signatures, qualitatively distinct from that of a single pair of Weyl nodes. In particular, we show that magnetic orders with different chiralities can give rise to different periods in LMC and PHC as a function of the in-plane magnetic field direction. This is ultimately related to differences in the symmetry-imposed constraints on the Weyl nodes.

I. INTRODUCTION

The discovery of large anomalous Hall effect (AHE) at room temperature in $\text{Mn}_3\text{X}(\text{Sn},\text{Ge})$ [1–3] has led to great interest in these materials from both a fundamental and an application point of view. Conventionally, a large AHE is associated with ferromagnetic metals, while Mn_3X materials are non-collinear AFMs. Thus, the discovery confirms the prediction of AHE in certain non-collinear AFMs [4, 5] due to non-vanishing Berry curvature when certain symmetries are absent.

Beyond the AHE, other novel transport phenomena, such as large anomalous Nernst effect, spin Nernst effect [6] and spin Hall effect [7] have been predicted and subsequently observed in Mn_3Sn [8, 9] and more recently in Mn_3Ge [10]. Moreover, first-principle calculations predict the existence of Weyl nodes in these materials [11, 12]. Although these Weyl nodes are not pinned to the chemical potential, the observation of a positive magnetoconductance in the presence of parallel electric and magnetic field provides possible evidence of the chiral anomaly [13]. Thus, these materials are possibly Weyl metals [14], where the Weyl nodes, though not pinned to the chemical potential, are close enough to it to produce observable transport signatures.

The use of AFM materials in spintronic devices has several advantages over their ferromagnetic counterparts [15, 16]. To list a few: (i) due to the lack of macroscopic magnetization the information stored in AFM devices is robust against stray fields and magnetic moments of neighboring elements. This allows for more compact packing of AFM spintronic devices, facilitating miniaturization. (ii) The characteristic frequencies of switching between different AFM states are several orders of magnitude higher than those of FM materials, which leads to faster dynamics [17]. In addition to the inherent advantages, related to AFM character, the non-trivial topology can further enrich the potential applications due to dis-

sipationless transport, associated with the topologically protected boundary states [18]. Thus, the interlinked combination of non-collinear antiferromagnetism, non-trivial topology, and novel transport phenomena make these materials of particular interest for spintronic devices. It is clear that underlying all these phenomena is the non-collinear magnetic order. This magnetic order and its relation to magnetotransport is the focus of this article.

$\text{Mn}_3\text{X}(\text{Sn}, \text{Ge})$ has a hexagonal crystal structure (space group $P6_3/mmc$) [19], where the magnetic Mn^{3+} ions arrange in two Kagome layers related by inversion symmetry and separated by half a c -axis lattice constant. The magnetic Mn^{3+} ions in the Kagome layer give rise to a 120° antiferromagnetic order that sets in at a Néel temperature $T_N \approx 380$ K. However, symmetry analysis predicts various candidate 120° AFM spin configurations, as shown in Fig. 1 (b)-(e), and unambiguously identifying a unique ground state can be challenging. This ambiguity may be partially resolved using spherical neutron polarimetry measurements, which demonstrate that two E_{1g} configurations, shown in Fig. 1 (d), (e), are equally likely ground states for Mn_3Sn [20], while $E_{1g}(A_y)$ configuration is the unambiguous ground state for Mn_3Ge [21].

Noticeably, the two E_{1g} configurations have the same sense of real-space spin rotation over a triangular plaquette (chirality) [22] and are related by rigid rotation of all the spins. In contrast, the B_{1g} and B_{2g} configurations have real-space spin chirality, opposite to that of the E_{1g} configurations. It is known that in presence of spin-orbit coupling, such co-planar configuration can lead to accumulation of Berry phase as an electron moves around the plaquette and can have strong influence on transport [23]. Hence for the opposite chirality, one can expect different transport signatures. Even if a unique zero-field ground state is unambiguously determined, the determination of temperature and magnetic field dependent magnetization is crucial to fully understand possible topological

responses such as the negative longitudinal magnetoresistance, photogalvanic effect, and the anomalous Nernst effect.

Here we present an extensive study of the temperature-dependent magnetic structure of Mn_3Ge using finite-temperature classical Monte Carlo and time-dependent integration of Landau-Lifshitz-Gilbert (LLG) equations. Our goal is to establish the temperature-dependent magnetic order and how it affects the electronic structure and therefore the magnetotransport. Consistent with the experimental Néel temperature, we find that magnetic order starts to set in below $T_N \sim 380\text{K}$ with large fluctuations (Goldstone modes) as the uniaxial anisotropy is very small. At higher temperature (but still below T_N), these fluctuations suppress long-range real-space chiral order. The degeneracy between the two chiralities is lifted due to a finite Dzyaloshinskii-Moriya interactions (DMI) and at lower temperature (around 200 K and below) long-range chiral order is established, consistent with the E_{1g} configuration. Using the symmetries, imposed by these magnetic configurations, incorporated in a model Weyl metal, we discuss longitudinal magnetoconductivity (LMC) and planar Hall conductivity (PHC) and show how a chirality-dependent switch in their periodicity might occur due to symmetry-constrained motion of the Weyl nodes. In particular, we show that while B_{1g} and B_{2g} configurations exhibit two-fold periodicity, the E_{1g} configuration can lead to higher-order periods. Interestingly, a recent temperature-dependent measurement of the longitudinal magnetoresistance with the current and magnetic field in the crystallographic ab plane and the magnetic field at some angle φ to the current in high-quality Mn_3Ge thin films reveals a striking temperature dependence of the magnetoresistance on the field angle [24, 25], which is consistent with our main theoretical findings.

The paper is organized as follows. In Sec. II, we describe the magnetic model and the computational methods and details. In Sec. III, we discuss our main numerical results of temperature dependent magnetism in detail. In Sec. III B, we discuss the calculation of LMC and PHC, using a model of a Weyl metal, which has the symmetry, imposed by the magnetic orders, discussed in Sec. III. We end with a summary of the results and concluding remarks in Sec. IV.

II. MODEL AND METHODS

For the atomistic simulations of magnetic order as function of temperature, we start with the model Heisenberg Hamiltonian H described by Chen *et al.* [26] (see Fig. 1). The model describes local moments located on the Mn sites with intra-plane near-neighbor AFM couplings J_2 between near-neighbor Mn sites on the same crystallographic c plane, inter-plane AFM couplings J_1 and inter-plane FM couplings J_4 ; in addition, there is an intra-plane near-neighbor DMI coupling D with the

unit DMI vector \mathbf{d}_{ij} connecting spins i and j (indicated by yellow and green triangles in Fig. 1) along the c axis, and a weak single-site uniaxial anisotropy with easy axes indicated by the dashed lines in Fig. 1. We use a Cartesian coordinate system with the x - and y -axes along the crystallographic a and b axes, and the z axis along the crystallographic c axis (out of the plane in Fig. 1, and write

$$H_M = \frac{J_1}{2} \sum_{1,ij} \mathbf{S}_i \cdot \mathbf{S}_j + \frac{J_2}{2} \sum_{2,ij} \mathbf{S}_i \cdot \mathbf{S}_j + \frac{J_4}{2} \sum_{4,ij} \mathbf{S}_i \cdot \mathbf{S}_j + \frac{D}{2} \sum_{D,ij} \mathbf{d}_{ij} \cdot (\mathbf{S}_i \times \mathbf{S}_j) - k \sum_i (\mathbf{S}_i \cdot \hat{n}_i)^2 - 2.5\mu_B \sum_i \mathbf{S}_i \cdot \mathbf{B}_{\text{ext}}, \quad (1)$$

where \mathbf{S}_i is the spin director at site i , the sums $1, ij$ etc indicates a sum over sites connected by the coupling J_1 , n_i is the anisotropy easy axis direction for site i , and \mathbf{B}_{ext} is an applied uniform external induction field.

We used an orthorhombic unit cell with 24 Mn atoms shown in Fig. 1 and the Vampire code [28] with typically a $4.4863 \text{ nm} \times 5.1803 \text{ nm} \times 2.0942 \text{ nm}$ supercell containing 3,000 atoms with periodic boundary conditions in most simulations, although we also used larger supercells up to $8.9726 \times 10.36066 \times 4.18841 \text{ nm}^3$ to ensure that our results were not affected by the choice of supercell. We employed both finite-temperature Monte Carlo (MC) simulations as well as direct integration of the stochastic Landau-Lifshitz-Gilbert (s-LLG) equation [29] both with and without atomistic dipolar interactions in the s-LLG, for the magnetization dynamics at finite temperatures, typically monitoring sublattice magnetization at the six sublattices denoted in Fig. 1. For thermal averages we would collect between 50,000 and 1,000,000 Monte Carlo steps per spin (MC simulations) or timesteps at 0.1 fs (s-LLG simulations). We used a dimensionless damping α in the s-LLG of $\alpha = 0.1$. This is typically a good choice for modeling equilibrium properties; we also note that this is not inconsistent with an observed large magnon damping in Mn_3Ge [26, 30]. We could not detect any discernible differences in the results obtained using MC or s-LLG with our without dipolar interactions. Instead, the main issue in the simulations was always to ensure that the system did not get trapped in a local equilibrium, and we carefully monitored instantaneous average energies at each temperature and field as well as sublattice magnetizations to eliminate simulations that were clearly trapped in a local equilibrium. Starting with the coupling constants given by Chen *et al.* [26], we first verified the Néel temperature at 365 K using standard Monte Carlo simulations with averages over 50,000 Monte Carlo steps per spin (MCS), slightly adjusting the coupling constants by about 10% from the values given by Chen *et al.* [26] (Table I). Note that in Eq. (1) we double-count the sites in the summations and correct with a factor of 1/2 which leads to a factor of 2 different from the values quoted by Chen *et al.* [26]. As is seen in Table I, J_2 and J_4 are much

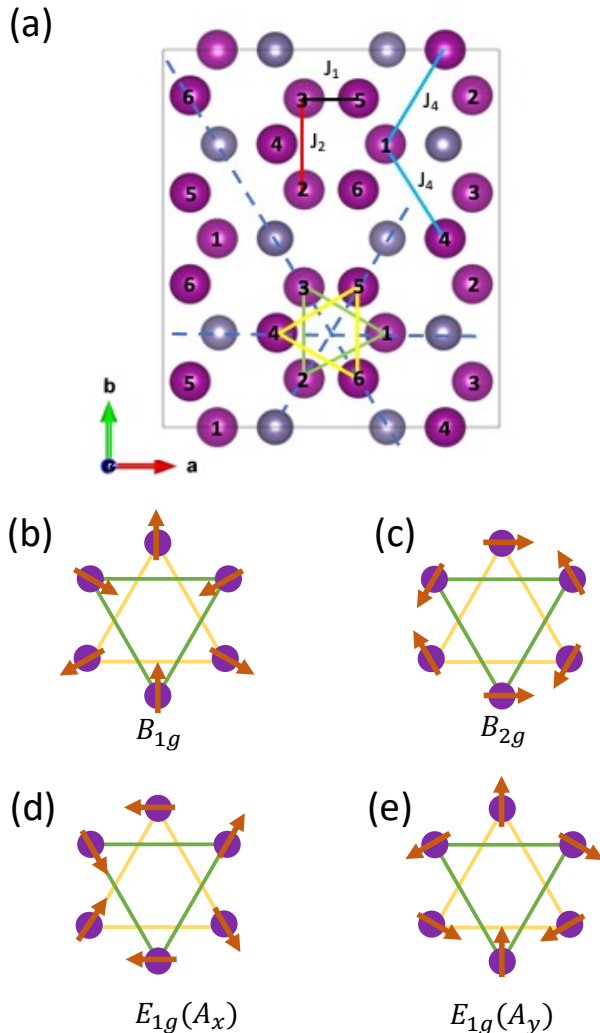


FIG. 1. (a) Orthorhombic Mn₃Ge unit cell used in the magnetic simulations (Crystal structure produced using VESTA [27]). The unit cell contains 24 Mn atoms on six different sublattices labeled 1 - 6. Sublattices 1 - 3 is on one crystallographic c -plane, and sublattices 4 - 6 on a different plane; the two sublattices form hexagons projected on the ab plane as indicated in the lower part of the figure with DMI coupling atoms 1-2-3 and atoms 4-5-6, as indicated by yellow and green triangles. In-plane AFM near-neighbor coupling J_2 , inter-plane near-neighbor AFM and inter-plane FM couplings J_1 and J_4 are indicated with red, black, and blue lines, respectively. Single-site uniaxial anisotropy directions are indicated by the dashed blue lines. (After Chen *et al.*[26].) (b)-(e) Different localized magnetic moment configuration allowed by 120° AFM order.

larger and control the Néel temperature; the anisotropy constant corresponds to a temperature of about 0.01 K and plays no role at all in the magnetic order down to temperatures ~ 0.1 K. This implies that the energy is continuously degenerate under in-plane rotations of all spins as the Hamiltonian only depends on relative angles

TABLE I. Coupling parameters for the magnetic model after Ref. [26]. The couplings are identified in Fig. 1 (a).

J_1 (meV)	J_2 (meV)	J_4 (meV)	k (meV)	D (meV)
6.24×10^{-3}	37.4	-18.7	1.0×10^{-3}	2.18×10^{-2}

of spins when the anisotropy can be ignored. The DMI constant D lifts the degeneracy between chiralities in a basic plaquette defined by sites 1 - 3 in Fig. 1. We shall see that even though D is small it affects the system on large temperature scales, ~ 100 K, as the coupling J_4 connects chiralities in different plaquettes.

We integrated the s-LLG equation for typically 10^7 time steps in steps of 0.1 fs at fixed temperatures from 0.1 K to 400 K, first randomizing the spins for 10^6 time steps at $T = 300$ K, after which we sampled sub-lattice spins every ten time steps. The simulations were run with no external field and with a 14 T field along the a -axis (Fig. 1) and at 30°, 45°, 60°, 75°, and 90° relative to the a -axis.

III. RESULTS AND DISCUSSION

A. Magnetic modeling: finite-temperature Monte Carlo and stochastic Landau-Lifshitz-Gilbert simulations

As the temperature is decreased below the Néel temperature, order sets in on the sub-lattices with the spins on a basic plaquette of three spins arranged in the classic in-plane Néel AFM order with an in-plane rotation of 120° between consecutive spins and the spin on a basic hexagon (sublattices 1 - 6 in Fig. 1) arranged in an octupolar order that transforms as the irreducible representation B_{2g} or E_{1g} (Fig. 1 (b) - (e)). The main difference between the two representations is that they have different chiralities: the E_{1g} order has positive chirality (as we move in the counter-clockwise direction around a basic plaquette of three spins, the spins rotate counter-clockwise) and the B_{2g} order has negative chirality. We calculate the magnetic chirality as $\hat{z} \cdot [\mathbf{S}_i \times \mathbf{S}_j]$, where \mathbf{S}_i and \mathbf{S}_j are two spins in an elementary triangular plaquette, with the order of i and j going counterclockwise. Because of the DMI, these two chiral orders are not degenerate, but at $T \gtrsim 250$ K thermal fluctuations destroy the long-range chiral order. As the temperature is lowered to below approximately 250 K, specific chiral order develops. Depending on initial conditions, any simulation at temperatures below 200 K or so would develop a definite chirality, but the chirality would differ from simulation to simulation. Figure 2 depicts the normalized mean-field chirality calculated as $2\hat{z} \cdot \mathbf{m}_i \times \mathbf{m}_j / \sqrt{3}$, with $i, j = 1, 2, i, j = 2, 3$, and $i, j = 3, 1$, and \mathbf{m}_i the thermal averages of the sublattice magnetization obtained in MC simulations with 100,000 MC steps per spin. The fig-

ure also shows the thermal average of the magnetization magnitude on sublattice 1 (it is the same on the other sublattices). The figure shows that sublattice magnetization magnitude goes to zero at about $T_N \approx 365$ K, with the typical finite-size rounding near T_N . In contrast, the mean-field chirality drops sharply to zero at temperatures well below T_N , in a range of temperatures from 280 K to 340 K (in the simulations depicted in Fig. 2, this range is about 340 K to 360 K). Furthermore, the mean-field chirality exhibits large fluctuations and varies considerably as function of temperature for $T \gtrsim 200$ K. We have also observed the chirality to change sign at temperatures $T \gtrsim 200$ K. This leads us to conclude that a robust chiral order sets in at temperatures $T \lesssim 200$ K, well below T_N , but that the chiral order is not a distinct order but a feature of the Néel order in this system. We estimate the energy difference between the two chiralities to be 0.08 meV/spin. This is a little larger than the DMI coupling of about 0.02 meV, but substantially smaller than the main couplings J_1 and J_2 . However, the fact that low-temperature simulations would be trapped in a specific chirality at temperatures much above D/k_B clearly indicates that the barrier for switching between chiralities is substantially larger than the energy difference, about 200 K, corresponding to about 20 meV. This is close to the ferromagnetic coupling J_4 : when long-range chiral order has developed, the energy cost to switch chirality involves breaking the J_4 coupling, which is responsible for stabilizing long-range chiral order.

We also examined in some detail the response of the magnetization to an external applied field. It was suggested by Kiyohara *et al.* [2] that the spin configuration in a basic hexagon (sublattice sites 1 - 6) will rotate easily when an applied external field is rotated in-plane due to the very small anisotropy. On the other hand, an observation made by Chen *et al.* [26] was that in the presence of an external magnetic field, a small *transverse* ferromagnetic component of about $0.2 \mu_B$ per Mn_3Ge unit is developed in response to the applied field. In our simulations, we do not see any evidence of spin rotation with the applied field direction. In fact, even at an applied field of 14 T, the sublattice magnetization direction is largely independent of the applied magnetic field. There is in general a small component of magnetization, less than $0.01 \mu_B$ per Mn at $T = 10$ K, induced by the magnetic field, that is along the direction of the magnetic field, with a deviation from the direction of the applied field of 1° or less. Figure 3 depicts the angle of the sublattice magnetization relative to the a axis for an external field of 14 T applied in plane at different angles to the a axis at $T = 10$ K obtained simulating the s-LLG and averaging over 1,000,000 time steps at 0.1 fs. For systems without any defects, neither MC nor the s-LLG simulations show any evidence of rotation of the sublattice magnetization. This is particularly clear in the s-LLG simulations; the MC simulations are, as is typically the case for these systems, less unequivocal. It is possible that extrinsic factors are responsible for observed or inferred rotations of

the magnetization with external field, in particular magnetic defects. In fact, Mn_3Ge is stable only when there is an excess of Mn, typically about 10%, occupying Ge sites [2, 26]. Such defects can couple ferro- or antiferromagnetically to nearby Mn ions, and there may also be longer-range Ruderman–Kittel–Kasuya–Yosida interactions that can be either ferromagnetic or antiferromagnetic. We chose a simple model in order to explore the effect of Mn substitutions on Ge sites. We substituted one Ge atom with a Mn atom and coupled it ferromagnetically to its nearest Mn neighbors. This corresponds to a defect concentration of about 4%. In this case, the simulations show a clear rotation of the sublattice magnetizations in response to rotation of the external field. In addition, there is now consistently a larger deviation, about 2° to 3° , between the induced moment and the direction of the applied field. The direction of the deviation also depends on the chirality of the system. While the magnitude of the induced transverse magnetic moment is much smaller than the transverse magnetization observed by Chen *et al.* [26], this suggests that the observed transverse magnetization arises from interaction with defects. Therefore, we believe that observed spin rotation with magnetic field as well as transverse components are likely the result of Mn defects on Ge sites. We note that the transverse moment we observe is much smaller than that observed by Chen *et al.*, but the defect concentration in our simulations is also smaller. It is not inconceivable that the effect of increasing defect density is not simply additive. Moreover, in our calculations the spins rotate along the magnetic field rotation directions. This is in contrast to Ref. [2] and Ref. [26], where spin rotation is in direction opposite to the magnetic field rotation. We remark that in our calculations, the extra Mn atom couples ferromagnetically with its nearest neighbors. It is possible that for antiferromagnetic coupling, or with the inclusion of longer-range interactions, the spin rotation is opposite sense to that of the magnetic field.

B. Magnetotransport

Given the results from our finite-temperature simulations of the magnetic order, we now discuss how the configuration of local magnetic moments in Mn_3X can influence the magnetotransport. Our focus is on the period of LMC and PHC as functions of the in-plane magnetic field direction. The observation of a large AHE [2, 3] and anomalous Nernst effect [10] in Mn_3Ge has been attributed to Weyl nodes. The presence of Weyl nodes near the chemical potential has also been shown in density functional theory calculations [11, 31]. Similar to the conventional anisotropic magnetoresistance (AMR) in a ferromagnetic metal [32], a pair of isotropic Weyl nodes can lead to an anisotropic LMC that has a $\cos^2 \varphi$ dependence as a function of field-current angle φ , when the applied magnetic field, current and the Weyl node pairs all lie in same plane [33]. Unlike conventional AMR,

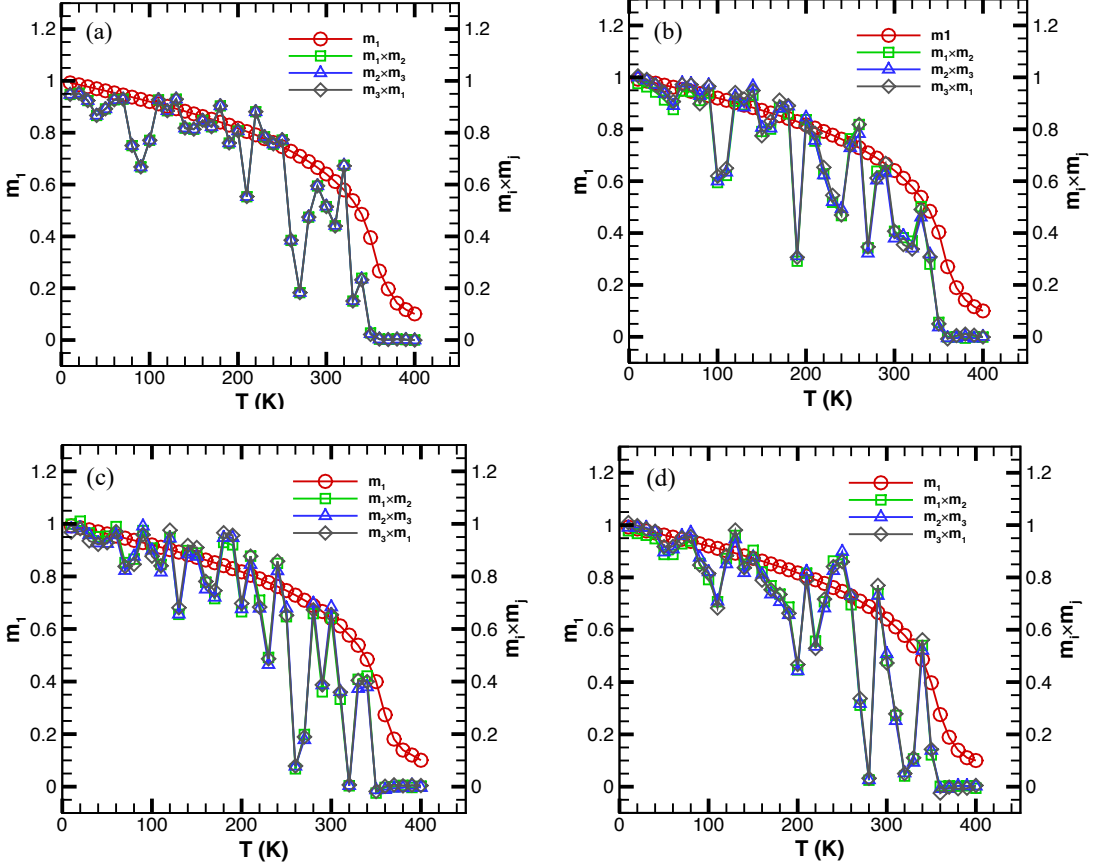


FIG. 2. Thermal average of the magnetization magnitude on sublattice 1 (red line and circle), and normalized mean-field chirality as a function of temperature for (a) no magnetic field, and 14 T field along (b) the a axis, (c) 30° to the a axis, and (d) 60° to the a axis. The different colors (green line and square, blue line and triangle, and grey line and diamond) denote the three different ways the chirality $\hat{z} \cdot (\mathbf{S}_i \times \mathbf{S}_j)$ can be calculated in an elementary triangular plaquette.

the chiral anomaly may be the reason behind these phenomena in a Weyl metal [33, 34]. If the Weyl nodes are tilted, the anisotropic LMC can develop a further $\cos \varphi$ component that can be the dominant component for the appropriate choice of Weyl node dispersion [35]. As a result the anisotropic LMC and closely related PHC can show a 2π -period in φ .

Here, using the specific symmetries of $\text{Mn}_3\text{X}(\text{Ge/Sn})$, we show that chiral anomaly induced LMC and PHC can also have more complex angular dependence. Starting with a simple model of a generic Weyl metal with tilted Weyl cones, we first derive the expression for the LMC and PHC as functions of the magnetic field direction. Then, using the symmetries of Mn_3X crystal, we enforce the corresponding constraints on the iso-energetic Weyl nodes and the Fermi surfaces around these nodes. Using these symmetry arguments, we show how the LMC and PHC signals and their periods can depend on temperature in these materials.

We start with a simple $\mathbf{k} \cdot \mathbf{p}$ Hamiltonian

$$H_\chi(\mathbf{k}) = \chi \hbar v \mathbf{k} \cdot \boldsymbol{\sigma} + \hbar t \cdot \mathbf{k} \sigma_0, \quad (2)$$

where $\chi = \pm$ denotes the chirality of the Weyl node, v is the Fermi velocity, \mathbf{t} is the tilt vector and $\boldsymbol{\sigma}$ are the Pauli matrices. We will only consider type- I nodes, which can be ensured by choosing $|\mathbf{t}| < v$. Under an external magnetic field \mathbf{B} and ignoring Landau quantization, the modified band energy

$$\epsilon_\tau^\chi(\mathbf{k}) = \hbar t_\chi \cdot \mathbf{k} + \tau \hbar v \mathbf{k} - g \mathbf{m}_{\tau, \mathbf{k}}^\chi \cdot \mathbf{B}, \quad (3)$$

that takes the orbital magnetization correction into account, where g is the orbital magnetization g -factor and

$$\mathbf{m}_{\tau, \mathbf{k}}^\chi = -\chi e v \frac{\tau \mathbf{k}}{2|\mathbf{k}|^2}, \quad (4)$$

is the orbital magnetic moment. Here $\tau = \pm$ denote the conduction and the valence band respectively. In our analysis, we take $\mathbf{B} = B(\cos \varphi, \sin \varphi, 0)$ and $\mathbf{t} = t(\cos \vartheta, \sin \vartheta, 0)$ in the xy plane (the ab -plane of Mn kagome layers).

Keeping the current direction fixed along the x -axis, for a pair of opposite chirality Weyl nodes lying in the xy -plane, the final expressions for the conductivity can

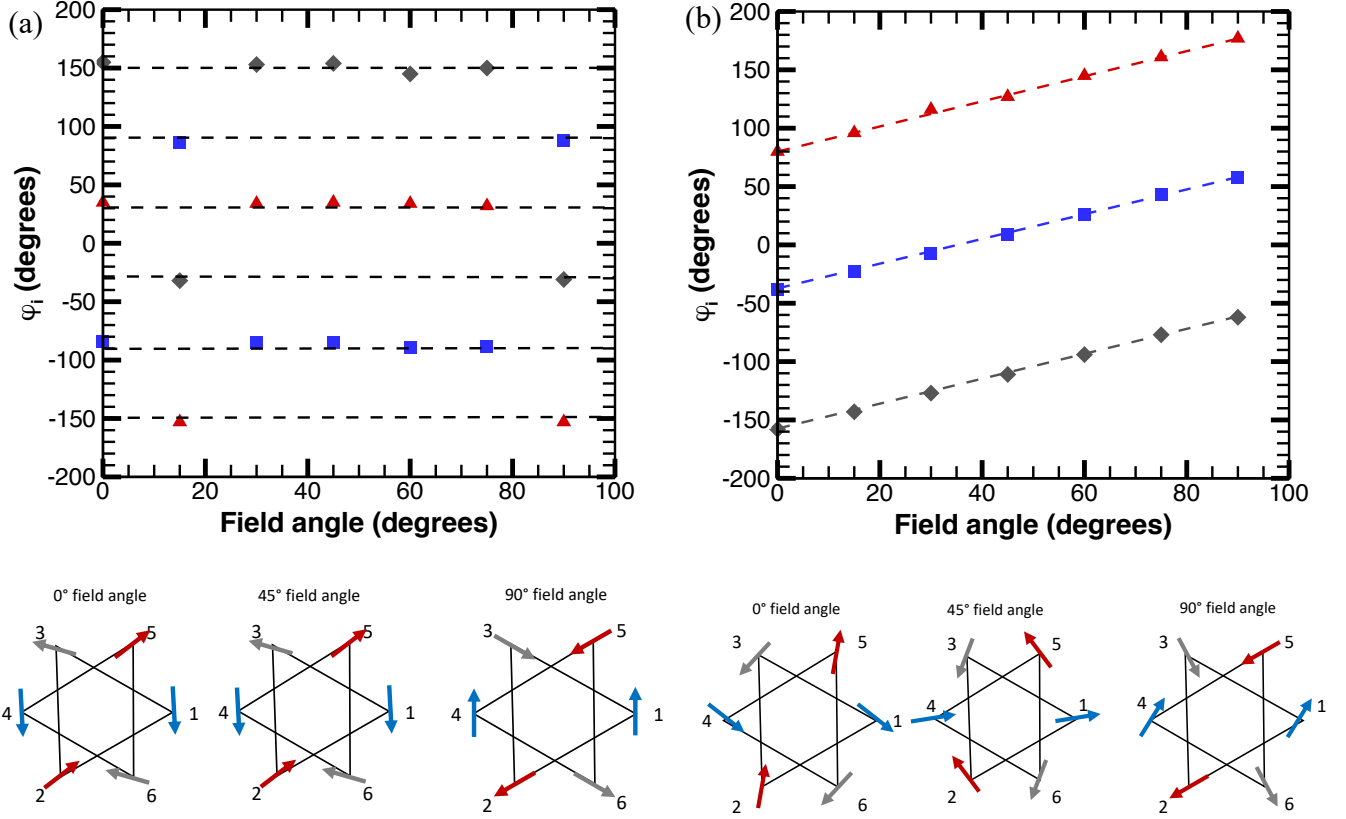


FIG. 3. Top row: Sublattice magnetization as function of applied magnetic field angle at $B = 14$ T and $T = 10$ K for (a) no magnetic defects, and (b) a small substitutional Mn defect on a Ge site, with sublattice 1 in blue, 2 in red, and 3 in gray; the orange dots and dashed line indicate a direction parallel to that of the applied field. The bottom row illustrates corresponding sublattice spin configurations at three different field angles. Without a magnetic defect, the low-temperature (ground state) spin configuration is the positive-chirality E_{1g} spin configuration (Fig. 1). With a magnetic defect present, the spins rotate uniformly with the magnetic field direction.

be summarized as follows (derivation is presented in the appendix A):

$$\sigma_{xx}^{\chi} = \sum_{n=0}^2 \sum_{m=-4}^4 a_{n,m}^{\chi} \cos(n\varphi + m\vartheta), \quad (5a)$$

$$\sigma_{xy}^{\chi} = \sum_{n=0}^2 \sum_{m=-4}^4 b_{n,m}^{\chi} \sin(n\varphi + m\vartheta), \quad (5b)$$

where n, m take integer values. The coefficients $a_{n,m}^{\chi}$ and $b_{n,m}^{\chi}$ depend on the magnetic field strength and on the band parameters such as μ, \mathbf{t}, v , and are listed in Eq. A9 and Eq. A10. In deriving Eq. 5, we have extended the results of Ref. [35] for arbitrary tilt direction and included the orbital magnetization corrections explicitly. We now incorporate the symmetries of the different magnetically-ordered states in Mn_3X in our transport calculations.

The top part of Fig. 4 (a), shows the $E_{1g}(A_x)$, magnetic configuration, where the vertices of the triangles represent the magnetic Mn-ions. This particular structure has inversion symmetry (I) along with mirror symmetries M_y, M_zT , and $M_x u_{1/2}T$, where T is the time reversal and $u_{1/2}$ is the translation by half lattice constant in z -direction. Next, we assume that the Fermi level lies near a reference Weyl node as shown in bottom part of Fig. 4 (a), with chirality $\chi = +$ and tilt $\mathbf{t} = t(\cos \vartheta, \sin \vartheta)$. Based on the symmetries listed above, all iso-energetic Weyl nodes are shown in the bottom part of Fig. 4 (a) with the red and green ellipses representing opposite chirality and the major axis of the ellipse along the tilt direction. By using a small \mathbf{k} -expansion around each of these Weyl nodes, we can write down a simple $\mathbf{k} \cdot \mathbf{p}$ Hamiltonian of the type shown in Eq. (2), with the details listed in Table II.

The magnetic configuration in the top part of Fig. 4

(b) can be obtained by starting from $E_{1g}(A_x)$ configu-

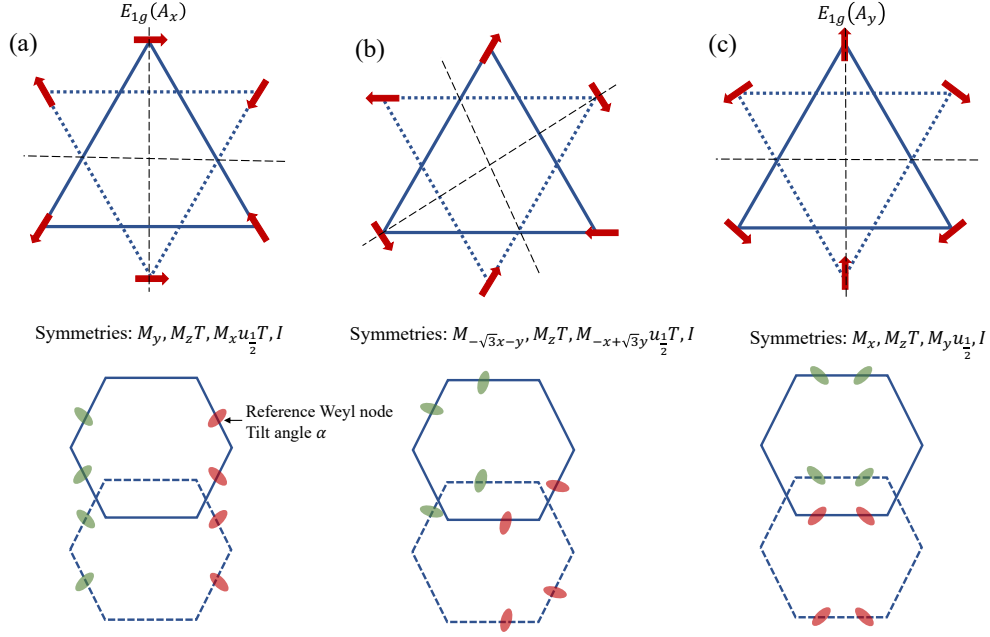


FIG. 4. A schematic representation of location of Weyl nodes as a function of localized spins for some high symmetry directions. The bottom panel shows all the symmetry-related Weyl nodes. The red and blue ovals represent Fermi surface around opposite chirality Weyl nodes with tilt. As all the localized spins are rotated simultaneously, the relevant label of crystalline symmetries change, which leads to movement of Weyl points.

TABLE II. Effective $\mathbf{k} \cdot \mathbf{p}$ near each Weyl node

Symmetry	$\mathbf{k} = (k_x, k_y, k_z)$	χ	$\boldsymbol{\Omega} = (\Omega_x, \Omega_y, \Omega_z)$	$\mathbf{t} = (t_x, t_y)$	$H = \chi \hbar v \mathbf{k} \cdot \boldsymbol{\sigma} + \hbar(t_x k_x + t_y k_y)$
M_y	$(-k_x, k_y, k_z)$	$-\chi$	$(\Omega_x, -\Omega_y, -\Omega_z)$	$(-t_x, t_y)$	$-\chi \hbar v \mathbf{k} \cdot \boldsymbol{\sigma} + \hbar(-t_x k_x + t_y k_y)$
$M_z T$	$(-k_x, -k_y, k_z)$	$-\chi$	$(\Omega_x, \Omega_y, -\Omega_z)$	$(-t_x, -t_y)$	$-\chi \hbar v \mathbf{k} \cdot \boldsymbol{\sigma} + \hbar(-t_x k_x - t_y k_y)$
$M_x u_{1/2} T$	$(-k_x, k_y, -k_z)$	$-\chi$	$(\Omega_x, -\Omega_y, \Omega_z)$	$(-t_x, t_y)$	$-\chi \hbar v \mathbf{k} \cdot \boldsymbol{\sigma} + \hbar(-t_x k_x + t_y k_y)$
I	$(-k_x, -k_y, -k_z)$	$-\chi$	$(\Omega_x, \Omega_y, \Omega_z)$	$(-t_x, -t_y)$	$-\chi \hbar v \mathbf{k} \cdot \boldsymbol{\sigma} + \hbar(-t_x k_x - t_y k_y)$

rotation and applying a counter-clockwise rotation of all the localized spins by $\pi/3$. As a result the mirror planes perpendicular the triangle rotate by the same angle but clockwise. The remaining symmetries, *i. e.* I and mirror in the triangular plane ($M_z T$) symmetries are still intact. The configuration in Fig. 4 (b) can also be viewed as an overall counter-clockwise rotation of the crystal by $2\pi/3$ followed by time reversal. As a result the Weyl nodes move to different positions in the momentum space as shown in the bottom panel of Fig. 4 (b). Similarly, Fig. 4 (c) shows when all spins are rotated by $\pi/2$ counter-clockwise, the perpendicular mirror planes rotate by $\pi/2$ -clockwise.

From the above analysis, it is clear that as the localized spins are rotated in a rigid fashion, the Weyl nodes must move in \mathbf{k} -space. Figure 4 only shows configurations in which spins are aligned along some high symmetry directions. However, if the spins are rigidly rotated in an arbitrary direction, the above-mentioned symmetries, apart from the I -symmetry, may all be broken. Hence,

in principle, the movement of Weyl nodes as function of spin rotation can be complicated. In the analysis below, we consider the simplest possible picture of Weyl nodes movement shown schematically in Fig. 5. We note that the positions of the Weyl nodes when the spins are aligned along high-symmetry directions are determined by symmetry irrespective of the particular model. As every localized spin is rotated by an angle δ , the movement of Weyl nodes can be thought of by rotating the momentum space around the origin by $-\delta$. The reference Weyl node as pointed out in Fig. 4 (a) is now at a new tilt angle $\vartheta - \delta$. Given this, next, we add the contribution to the conductivity from all the eight iso-energy Weyl nodes according to Eq. 5, and after some manipulation obtain

$$\sigma_{xx} = \sum_{n=0}^6 \bar{a}_n \cos(n\varphi) \quad (6a)$$

$$\sigma_{xy} = \sum_{n=1}^6 \bar{b}_n \sin(n\varphi). \quad (6b)$$

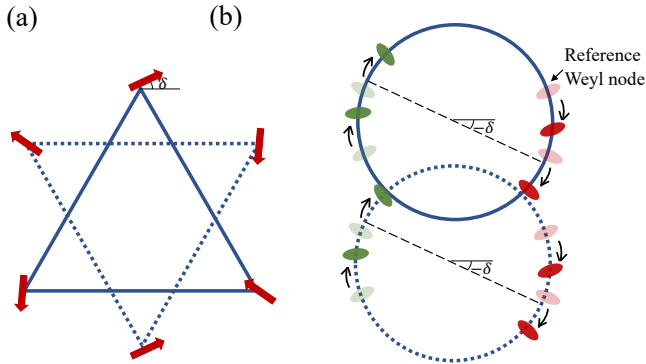


FIG. 5. A schematic representation of location of Weyl nodes as a function of localized spins, (a) Rotation of localized spins, (b) Corresponding movement of Weyl nodes. The shaded ovals are at the original location of Weyl nodes and the solid ovals are at the new locations. As all the localized spins are rotated simultaneously, the Weyl nodes move because of change in mirror planes.

$$\bar{a}_n = \begin{cases} 4 \sum'_m \sum_{\chi=\pm} \chi^m (a_{n+m,m}^x + a_{m-n,m}^x) \cos(m\vartheta) & \delta = \varphi \\ 4 \sum'_m \sum_{\chi=\pm} \chi^m (a_{n-m,-m}^x + a_{-m-n,-m}^x) \cos(m\vartheta) & \delta = -\varphi \end{cases} \quad (7a)$$

$$\bar{b}_n = \begin{cases} 4 \sum'_m \sum_{\chi=\pm} \chi^m (b_{n+m,m}^x - b_{m-n,m}^x) \cos(m\vartheta) & \delta = \varphi \\ 4 \sum'_m \sum_{\chi=\pm} \chi^m (b_{n-m,-m}^x - b_{-m-n,-m}^x) \cos(m\vartheta) & \delta = -\varphi. \end{cases} \quad (7b)$$

Here the \sum' sums over the certain values of $m \in [-4, 4]$, such that the first subscript $p \in [0, 2]$ for $a_{p,m}^x$ and $b_{p,m}^x$. The most important observation is that the higher order (up to six-fold) components generically emerge in the angular dependence of the LMC and PHC signals as a function of the magnetic field direction φ . This dependence is a direct consequence of the movement of tilted Weyl nodes in \mathbf{k} -space. The movement of Weyl nodes in \mathbf{k} -space is ensured because of change in the underlying symmetries due to spin rotation. Such a spin rotation in response to an external field has been suggested as a consequence of coupling of the octupolar order to the external field [26, 36]. We did not observe that in our finite-T simulations without disorder. We note however that our simple model of substitutional disorder of Mn on Ge sites [see Fig. 3 (b)] suggests that substitutions of Mn on Ge sites can lead to such rotations.

For isotropic Weyl nodes, the movement of the nodes in \mathbf{k} space does not contribute any additional angular dependence and we obtain the familiar $\cos(2\varphi)$ and $\sin(2\varphi)$ angular dependence in LMC and PHC respectively [33]. Moreover, for the simple tilted Weyl nodes considered here the coefficients $a_{n,m}^x$ and $b_{n,m}^x$ are such that only even n components are non-zero in the conductivity expressions in Eq. 6. If the real space spin chirality is

Here, we have assumed that the spin rotation δ either follows the magnetic field rotation φ (i.e. $\delta = \varphi$) as we find in our case or it is opposite to magnetic field rotation (i.e. $\delta = -\varphi$) as found in Ref. [2] and Ref. [26]. Depending on the situation, we obtain the coefficients

switched to B_{1g} or B_{2g} as shown in Fig. 1 (b), (c), the structure gains an additional C_{3z} rotation symmetry, while I , M_y , M_zT , and $M_x u_{1/2}T$ are still intact. As a result there are total 24 iso-energy Weyl nodes (where the additional nodes are due to C_{3z} symmetry). Following the previous analysis, adding the contribution of all these Weyl nodes and taking into account movement of the nodes, we obtain

$$\sigma_{xx} = 24a_{0,0}^+ + 24a_{2,0}^+ \cos(2\varphi), \quad (8a)$$

$$\sigma_{xy} = 24b_{2,0}^+ \sin(2\varphi). \quad (8b)$$

Notice that, while the expressions of the coefficients $a_{n,m}^x$ and $b_{n,m}^x$ as presented in Eqs. A9, A10 are specific to the tilted Weyl node model considered here, the general conductivity expressions in Eqs. 6, 7, and 8 are independent of this detail and are obtained entirely from symmetries.

Now we are in position to discuss possible transport signatures that can be related to the chiral order that sets up at temperatures T around 200 K. A period-two LMC is expected in conventional ferromagnetic metal. Since above 200 K no long range chiral order is established, it is possible that in this regime the LMC has non-topological origin due to a finite magnetization [32]. However, any

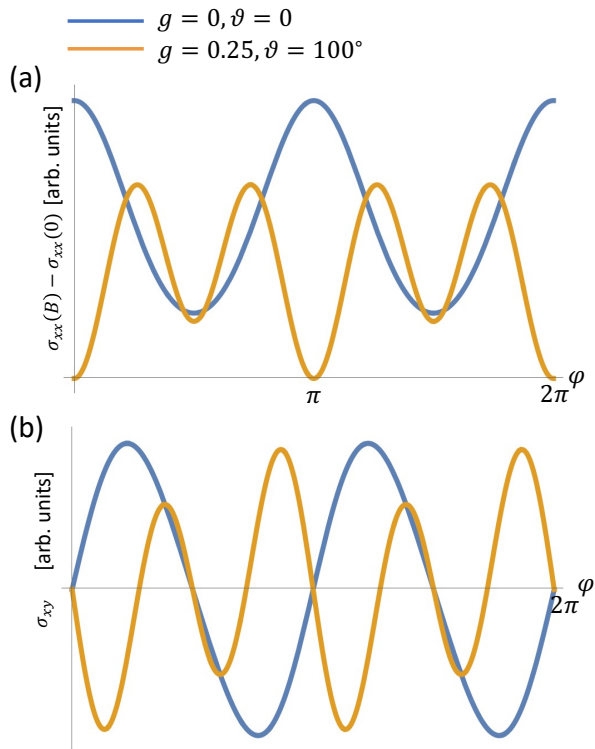


FIG. 6. Two-fold and four-fold period in the (a) LMC and (b) PHC for the E_{1g} configuration based on appropriate choice of band parameters. We have chosen $t/v = 0.2$, $\mu = 20$ meV, $v = 2$ meV, and $B = 10T$ for both cases. For period the case with finite period four component (orange), we have chosen $g = 0.25, \vartheta = 100^\circ$ and for the case with only period two component (blue), we have chosen $g = 0, \vartheta = 0^\circ$.

remnant zero-field magnetic moment is very small. The other possibility is that in the absence of long-range chiral order, the combined effect of both chiralities leads to a dominant period-two angular dependence of LMC and PHC. As the temperature is decreased and E_{1g} chiral order is set below $T \approx 200$ K, the underlying $\mathbf{k} \cdot \mathbf{p}$ expansion near iso-energy Weyl nodes is set by band parameters such that higher period LMC and PHC becomes dominant. In the C_{3z} -symmetry broken E_{1g} phase, along with the change in period, the phase of the LMC and PHC signal can also change depending on the tilt angle ϑ and other band parameters. This can be seen in the Fig. 6, where for the case with finite period four component (orange curves), we have chosen parameters such that the LMC has a minima when the field is parallel to current. Thus maxima of the LMC need not be at $\varphi = 0$ (when current and magnetic field are in same direction) as expected from chiral anomaly. It is important to note that although in our Eq. (6) there are finite period-six contribution, because $t^4/v^4 \ll 1$, we do not find dominant period-six LMC and PHC signal for any choice of band parameters. Thus our proposed increased period to four is only meant to point to a possible mechanism, since we assumed a simplified Weyl node model with elliptical

Fermi surface from a single tilt vector. In a real system, the relevant Fermi surface around each Weyl node can be more complicated.

IV. CONCLUSION

In conclusion, we have sought to elucidate the connection between magnetic order and magnetotransport in Mn_3Ge . We performed detailed atomistic simulations of the temperature dependent magnetic order of and found a Néel temperature $T_N \approx 365$ K, which is consistent with experiments. The frustrated 120° AFM configuration found in this system has different competing magnetic orders that are allowed by symmetries and are distinguished by the sense of rotation of localized spins over an elementary triangular plaquette (chirality). We find that for high temperatures, but well below T_N , thermal fluctuations suppress long-range chiral order. At a lower temperature (~ 200 K) long range chiral order is established. We also studied the effect of magnetic field in the ab -plane on the local magnetic moments. We found that for defect-free systems even in high magnetic field, the magnetic moments do not rotate with the magnetic field. However, for a system with a small defect concentration, the magnetic field can rotate moments on each site.

Based on the results of the atomistic simulations, we discuss possible distinction between transport signatures associated with different chiral orders. Using a simple tilted Weyl node model along with the crystalline symmetries of different chiral orders, we show that a chiral anomaly-induced anisotropic LMC and PHC for the E_{1g} magnetic order can acquire angular dependencies [$\cos(4\varphi)$ and $\cos(6\varphi)$ terms] that are different from the previously obtained one [33, 35], while the B_{1g} and B_{2g} orders do not acquire these additional angular dependencies. In our transport analysis, the additional angular dependence comes from the motion of the Weyl nodes in the \mathbf{k} -space, which is guaranteed from spin rotation and crystal symmetries.

Anisotropic LMC and PHC can also originate purely from the orbital effects of extremely anisotropic Fermi surfaces [37–39], where the exact angular dependence is set by the type of lattice and the microscopic details of the Fermi surface. Although this orbital origin requires extreme anisotropy of the Fermi surface, it cannot be ruled out entirely. In fact the additional angular dependency acquired by the movement of the Fermi-pocket in the \mathbf{k} -space can appear in such cases as well. Deeper understanding of the origin of anisotropic LMC and PHC in these materials is an interesting future direction to pursue and important for potential applications that exploit the AHE or spin injection in heterostructures. Progress in this direction can potentially be achieved by experiments that study in detail the evolution of the amplitude of angular LMC and PHC with magnetic field and chemical potential via different doping or by gating thin films.

V. ACKNOWLEDGEMENT

We are thankful to Deshun Hong and Anand Bhattacharya for numerous discussions and sharing their unpublished results. This work was supported the Center for the Advancement of Topological Semimetals, an Energy Frontier Research Center funded by the U.S. Department of Energy Office of Science, Office of Basic Energy Sciences. Research at Perimeter Institute is supported in part by the Government of Canada through the Department of Innovation, Science and Economic Development and by the Province of Ontario through the Ministry of Economic Development, Job Creation and Trade. We gratefully acknowledge the computing resources provided on Bebop and Blues, high-performance computing clusters operated by the Laboratory Computing Resource Center at Argonne National Laboratory.

Appendix A: Derivation of LMC and PHC

In this section we derive the expressions for LMC and PHC used in the main text. Under the semiclassical Boltzmann theory, the contribution to the current density in the vicinity of a Weyl node is

$$\mathbf{J}_\chi = -e \int \frac{d^3k}{(2\pi)^3} D_\chi^{-1} \dot{\mathbf{r}}_\chi f_{\mathbf{k}}^\chi(\mathbf{r}), \quad (\text{A1})$$

where $\dot{\mathbf{r}}_\chi$ is the group velocity of the semiclassical wave packet, $f_{\mathbf{k}}^\chi(\mathbf{r})$ is the distribution function of the electron under applied weak external field, and $D_\chi(\mathbf{B}, \boldsymbol{\Omega}_{\mathbf{k}}^\chi) = [1 + (e/\hbar)(\mathbf{B} \cdot \boldsymbol{\Omega}_{\mathbf{k}}^\chi)]^{-1}$ is the phase space volume factor and

$$\boldsymbol{\Omega}_{\mathbf{k}}^\chi = -\chi \frac{\mathbf{k}}{2|\mathbf{k}|^3}, \quad (\text{A2})$$

is the momentum space Berry-curvature in the conduction band $\tau = +$. Since our derivation is at the fixed Fermi level, where only one of the band will have finite

contribution, it suffices to the fix $\tau = +$ by choosing to work in the conduction band. Under the external electric field \mathbf{E} , the semiclassical wave packet dynamics leads to the equations of motion:

$$\dot{\mathbf{r}}_\chi = \frac{1}{\hbar} \nabla_{\mathbf{k}} \epsilon_{\mathbf{k}}^\chi - \dot{\mathbf{k}}_\chi \times \boldsymbol{\Omega}_{\mathbf{k}}^\chi, \quad (\text{A3a})$$

$$\dot{\mathbf{k}}_\chi = -\frac{e}{\hbar} \mathbf{E} - \frac{e}{\hbar} \dot{\mathbf{r}}_\chi \times \mathbf{B}. \quad (\text{A3b})$$

Substituting Eq. A3b in Eq. A3a, we obtain

$$\dot{\mathbf{r}}_\chi = D_\chi(\mathbf{B}, \boldsymbol{\Omega}_\chi) \left[\mathbf{v}_{\mathbf{k}}^\chi + \frac{e}{\hbar} \mathbf{E} \times \boldsymbol{\Omega}_{\mathbf{k}}^\chi + \frac{e}{\hbar} (\mathbf{v}_{\mathbf{k}}^\chi \cdot \boldsymbol{\Omega}_{\mathbf{k}}^\chi) \mathbf{B} - \frac{e}{\hbar} \boldsymbol{\Omega}_{\mathbf{k}}^\chi \cdot (\dot{\mathbf{k}}_\chi \times \boldsymbol{\Omega}_{\mathbf{k}}^\chi) \mathbf{B} \right], \quad (\text{A4})$$

where

$$\mathbf{v}_{\mathbf{k}}^\chi = \frac{1}{\hbar} \nabla_{\mathbf{k}} \epsilon_{\mathbf{k}}^\chi = \mathbf{t} + v \hat{\mathbf{k}} + 4gv \frac{e}{\hbar} (\mathbf{B} \cdot \boldsymbol{\Omega}_{\mathbf{k}}^\chi) \hat{\mathbf{k}} + \frac{\chi g e v}{2\hbar |\mathbf{k}|^2} \mathbf{B} \quad (\text{A5})$$

is the Fermi velocity. Up to linear order, we can ignore the last term on the RHS of Eq. A4.

The distribution function is calculated from the Boltzmann equation under steady state and relaxation-time approximation, i.e. $\dot{\mathbf{k}}_\chi \cdot \partial_{\mathbf{k}} f_{\mathbf{k}}^\chi(\mathbf{r}) = (f_{\text{eq}}^\chi - f_{\mathbf{k}}^\chi(\mathbf{r}))/\tau_{\mathbf{k}}$. The distribution function then can be obtained as

$$f_{\mathbf{k}}^\chi = f_{\text{eq}}^\chi + \left[e D^\chi \tau_{\mathbf{k}} \mathbf{E} \cdot \mathbf{v}_{\mathbf{k}}^\chi + \frac{e^2}{\hbar} D^\chi \tau_{\mathbf{k}} (\mathbf{B} \cdot \mathbf{E}) (\mathbf{v}_{\mathbf{k}}^\chi \cdot \boldsymbol{\Omega}_{\mathbf{k}}^\chi) + \hat{v}_{\mathbf{k}}^\chi \cdot \boldsymbol{\Gamma}^\chi \right] \frac{\partial f_{\text{eq}}^\chi}{\partial \epsilon^\chi}. \quad (\text{A6})$$

Here the third term on RHS is a correction factor due to magnetic field \mathbf{B} . The correction factor $\boldsymbol{\Gamma}$ follows complicated coupled equations, which are obtained in Ref. [33]. However, Ref. [35] shows its contribution to conductivity up to 2nd order in magnetic field vanishes. Hence, from now on we ignore the correction factor $\boldsymbol{\Gamma}$.

After substituting Eq. A4 and Eq. A6 in the current density Eq. A1, we obtain

$$\begin{aligned} \mathbf{J}_\chi = & -\frac{e^2 \tau}{(2\pi)^3} \int d^3k \frac{\partial f_{\text{eq}}^\chi}{\partial \epsilon^\chi} D^\chi \left[\mathbf{v}_{\mathbf{k}}^\chi + \frac{e}{\hbar} (\mathbf{v}_{\mathbf{k}}^\chi \cdot \boldsymbol{\Omega}_{\mathbf{k}}^\chi) \mathbf{B} \right] \left[\mathbf{v}_{\mathbf{k}}^\chi + \frac{e}{\hbar} (\mathbf{v}_{\mathbf{k}}^\chi \cdot \boldsymbol{\Omega}_{\mathbf{k}}^\chi) \mathbf{B} \right] \cdot \mathbf{E} \\ & - \frac{e^2 \tau}{(2\pi)^3} \int d^3k \frac{\partial f_{\text{eq}}^\chi}{\partial \epsilon^\chi} D^\chi \frac{e}{\hbar} (\mathbf{E} \times \boldsymbol{\Omega}_{\mathbf{k}}^\chi) \left[\mathbf{v}_{\mathbf{k}}^\chi + \frac{e}{\hbar} (\mathbf{v}_{\mathbf{k}}^\chi \cdot \boldsymbol{\Omega}_{\mathbf{k}}^\chi) \mathbf{B} \right] \cdot \mathbf{E} \\ & - \frac{e^2}{\hbar (2\pi)^3} \int d^3k (\mathbf{E} \times \boldsymbol{\Omega}_{\mathbf{k}}^\chi) f_{\text{eq}}^\chi. \end{aligned} \quad (\text{A7})$$

Here, we have assumed that scattering rate is independent of momentum. The second line in the above expression is $O(E^2)$, which we ignore in the linear theory

discussed here. The last line above contains the contribution from the occupied states, which is only finite for the transverse current. In that case, it corresponds to

the anomalous Hall current. Since, it is not of interest for the discussion here, we ignore this part as well. From the first line, we can write down the conductivity tensor

$$\boldsymbol{\sigma}^{\chi} = \frac{e^2\tau}{(2\pi)^3} \int d^3k D^{\chi} \left[\mathbf{v}_{\mathbf{k}}^{\chi} + \frac{e}{\hbar} (\mathbf{v}_{\mathbf{k}}^{\chi} \cdot \boldsymbol{\Omega}_{\mathbf{k}}^{\chi}) \mathbf{B} \right] \left[\mathbf{v}_{\mathbf{k}}^{\chi} + \frac{e}{\hbar} (\mathbf{v}_{\mathbf{k}}^{\chi} \cdot \boldsymbol{\Omega}_{\mathbf{k}}^{\chi}) \mathbf{B} \right] \delta(\epsilon_{\mathbf{k}}^{\chi} - \mu). \quad (\text{A8})$$

Here, μ is the chemical potential. In writing down Eq. A8, we have taken the zero temperature limit and replaced the energy derivative of the equilibrium distri-

bution function with the δ -function. The final expression can be written in the form of Eq. 5. Notice that although, we have used the simple tilted Weyl node for simplicity, the expression in Eq. 5 is more general and valid for more complicated Fermi surface surrounding the Weyl node. For the simple case of tilted Weyl node where the Fermi surface around the node is an ellipsoid, we can carry out the integrals in Eq. A8 analytically in spherical coordinates by explicitly expanding the integrand up to second order in the magnetic field. The final expressions for the non-zero coefficients [up to the prefactor $e^2\tau/(2\pi)^3$] are as follows:

$$a_{0,0}^{\chi} \equiv a_{0,0} = -\frac{\pi g e^2 B^2 v^2}{\hbar^2} - \frac{2\pi(t^2 - 2v^2)\mu^2}{3\hbar^2 v^2} + \frac{\pi e^2 B^2 v^2 t^2}{210\mu^2} \left[\frac{14t^2}{v^2} - 156 + 492g + 115g^2 + \frac{63v^2}{t^2} + \frac{371gv^2}{t^2} + \frac{273g^2 v^2}{t^2} \right] \quad (\text{A9a})$$

$$a_{0,2}^{\chi} \equiv a_{0,2} = -\frac{2\pi\mu^2 t^2}{3\hbar^2 v^2} - \frac{\pi e^2 B^2 v^2 t^2}{210\mu^2} \left[\frac{7t^2}{v^2} + 50 - 309g - 40g^2 \right] \quad (\text{A9b})$$

$$a_{1,1}^{\chi} = a_{1,-1}^{\chi} = \chi a_{1,-1} = -\frac{2\pi\chi e v B t (3 + g)}{3\hbar} \quad (\text{A9c})$$

$$a_{2,0}^{\chi} \equiv a_{2,0} = -\frac{\pi g e^2 B^2 v^2}{\hbar^2} + \frac{\pi e^2 B^2 v^2 t^2}{420\mu^2} \left[\frac{7t^2}{v^2} - 455 + 1304g + 38g^2 + \frac{98v^2}{t^2} + \frac{966gv^2}{t^2} + \frac{98g^2 v^2}{t^2} \right] \quad (\text{A9d})$$

$$a_{2,-2}^{\chi} \equiv a_{2,-2} = -\frac{\pi e^2 B^2 t^4}{15\mu^2} + \frac{\pi e^2 B^2 v^2 t^2}{210\mu^2} \left[-113 + 421g + 40g^2 \right] \quad (\text{A9e})$$

$$a_{2,-4}^{\chi} \equiv a_{2,-4} = \frac{\pi e^2 t^4 B^2}{60\mu^2} \quad (\text{A9f})$$

and

$$b_{0,2}^{\chi} \equiv b_{0,2} = -\frac{2\pi\mu^2 t^2}{3\hbar^2 v^2} - \frac{\pi e^2 B^2 v^2 t^2}{210\mu^2} \left[\frac{7t^2}{v^2} + 50 - 309g - 40g^2 \right] \quad (\text{A10a})$$

$$b_{1,-1}^{\chi} = \chi b_{1,-1} = \frac{4\pi\chi e v B t g}{3\hbar} \quad (\text{A10b})$$

$$b_{1,1}^{\chi} = \chi b_{1,1} = \frac{2\pi\chi e v B t (g - 3)}{3\hbar} \quad (\text{A10c})$$

$$b_{2,0}^{\chi} \equiv b_{2,0} = -\frac{\pi g e^2 B^2 v^2}{\hbar^2} + \frac{\pi e^2 B^2 v^2 t^2}{420\mu^2} \left[\frac{7t^2}{v^2} - 405 + 1304g + 38g^2 + \frac{98v^2}{t^2} + \frac{966gv^2}{t^2} + \frac{98g^2 v^2}{t^2} \right] \quad (\text{A10d})$$

$$b_{2,-2}^{\chi} \equiv b_{2,-2} = -\frac{\pi e^2 B^2 t^4}{15\mu^2} + \frac{\pi e^2 B^2 v^2 t^2}{210\mu^2} \left[-113 + 421g + 40g^2 \right] \quad (\text{A10e})$$

$$b_{2,-4}^{\chi} \equiv b_{2,-4} = -\frac{\pi e^2 B^2 t^4}{60\mu^2} \quad (\text{A10f})$$

[1] S. Nakatsuji, N. Kiyohara, and T. Higo, “Large anomalous hall effect in a non-collinear antiferromagnet at room

temperature,” *Nature* **527**, 212 (2015).

- [2] N. Kiyohara, T. Tomita, and S. Nakatsuji, “Giant anomalous hall effect in the chiral antiferromagnet Mn_3Ge ,” *Phys. Rev. Appl.* **5**, 064009 (2016).
- [3] A. K. Nayak, J. E. Fischer, Y. Sun, B. Yan, J. Karel, A. C. Komarek, C. Shekhar, N. Kumar, W. Schnelle, J. Kübler, C. Felser, and S. P. Parkin, “Large anomalous hall effect driven by a nonvanishing berry curvature in the noncollinear antiferromagnet Mn_3Ge ,” *Sci. Adv.* **2** (2016), 10.1126/sciadv.1501870.
- [4] H. Chen, Q. Niu, and A. H. MacDonald, “Anomalous hall effect arising from noncollinear antiferromagnetism,” *Phys. Rev. Lett.* **112**, 017205 (2014).
- [5] J. Kübler and C. Felser, “Non-collinear antiferromagnets and the anomalous hall effect,” *EPL* **108**, 67001 (2014).
- [6] G.-Y. Guo and T.-C. Wang, “Large anomalous nernst and spin nernst effects in the noncollinear antiferromagnets Mn_3X ($\text{X} = \text{Sn}, \text{Ge}, \text{Ga}$),” *Phys. Rev. B* **96**, 224415 (2017).
- [7] Y. Zhang, Y. Sun, H. Yang, J. Železný, S. P. P. Parkin, C. Felser, and B. Yan, “Strong anisotropic anomalous hall effect and spin hall effect in the chiral antiferromagnetic compounds Mn_3x ($x = \text{Ge}, \text{Sn}, \text{Ga}, \text{Ir}, \text{Rh}, \text{and Pt}$),” *Phys. Rev. B* **95**, 075128 (2017).
- [8] M. Ikhlas, T. Tomita, T. Koretsune, M.-T. Suzuki, D. Nishio-Hamane, R. Arita, Y. Otani, and S. Nakatsuji, “Large anomalous nernst effect at room temperature in a chiral antiferromagnet,” *Nat. Phys.* **13**, 1085 (2017).
- [9] M. Kimata, H. Chen, K. Kondou, S. Sugimoto, P. K. Muduli, M. Ikhlas, Y. Omori, T. Tomita, A. H. MacDonald, S. Nakatsuji, and Y. Otani, “Magnetic and magnetic inverse spin hall effects in a non-collinear antiferromagnet,” *Nature* **565**, 627 (2019).
- [10] D. Hong, N. Anand, C. Liu, H. Liu, I. Arslan, J. E. Pearson, A. Bhattacharya, and J. S. Jiang, “Large anomalous nernst and inverse spin-hall effects in epitaxial thin films of kagome semimetal Mn_3Ge ,” *Phys. Rev. Mater.* **4**, 094201 (2020).
- [11] H. Yang, Y. Sun, Y. Zhang, W.-J. Shi, S. S. P. Parkin, and B. Yan, “Topological weyl semimetals in the chiral antiferromagnetic materials mn_3ge and mn_3sn ,” *New J. Phys.* **19**, 015008 (2017).
- [12] J. Kübler and C. Felser, “Weyl fermions in antiferromagnetic Mn_3Sn and Mn_3Ge ,” *EPL* **120**, 47002 (2017).
- [13] K. Kuroda, T. Tomita, M. T. Suzuki, C. Bareille, A. A. Nugroho, P. Goswami, M. Ochi, M. Ikhlas, M. Nakayama, S. Akebi, R. Noguchi, R. Ishii, N. Inami, K. Ono, H. Kumigashira, A. Varykhalov, T. Muro, T. Koretsune, R. Arita, S. Shin, T. Kondo, and S. Nakatsuji, “Evidence for magnetic weyl fermions in a correlated metal,” *Nat. Mater.* **16**, 1090 (2017).
- [14] A. A. Burkov, “Weyl metals,” *Annu. Rev. Condens. Matter Phys.* **9**, 359 (2018).
- [15] T. Jungwirth, X. Marti, P. Wadley, and J. Wunderlich, “Antiferromagnetic spintronics,” *Nat. Nanotechnol.* **11**, 231 (2016).
- [16] E. V. Gomonay and V. M. Loktev, “Spintronics of antiferromagnetic systems (review article),” *Low Temp. Phys.* **40**, 17 (2014).
- [17] M. Fiebig, N. P. Duong, T. Satoh, B. B. Van Aken, K. Miyano, Y. Tomioka, and Y. Tokura, “Ultrafast magnetization dynamics of antiferromagnetic compounds,” *J. Phys. D Appl. Phys.* **41**, 164005 (2008).
- [18] L. Šmejkal, Y. Mokrousov, B. Yan, and A. H. MacDonald, “Topological antiferromagnetic spintronics,” *Nat. Phys.* **14**, 242 (2018).
- [19] E. Krén, J. Paitz, G. Zimmer, and É. Zsoldos, “Study of the magnetic phase transformation in the Mn_3Sn phase,” *Physica B+C* **80**, 226 (1975).
- [20] P. J. Brown, V. Nunez, F. Tasset, J. B. Forsyth, and P. Radhakrishna, “Determination of the magnetic structure of Mn_3Sn using generalized neutron polarization analysis,” *J. Phys.: Condens. Matter* **2**, 9409 (1990).
- [21] J.-R. Soh, F. de Juan, N. Qureshi, H. Jacobsen, H.-Y. Wang, Y.-F. Guo, and A. T. Boothroyd, “Ground-state magnetic structure of Mn_3Ge ,” *Phys. Rev. B* **101**, 140411(R) (2020).
- [22] This chirality should be distinguished from the scalar spin chirality $\mathbf{S}_i \cdot \mathbf{S}_j \times \mathbf{S}_k$.
- [23] S.-S. Zhang, H. Ishizuka, H. Zhang, G. B. Halász, and C. D. Batista, “Real-space berry curvature of itinerant electron systems with spin-orbit interaction,” *Phys. Rev. B* **101**, 024420 (2020).
- [24] D. Hong, C. Liu, H.-W. Hsiao, J.-M. Zuo, H. Liu, I. Arslan, J. Pearson, J. Jiang, and A. Bhattacharya, “Epitaxial growth of kagome semimetal Mn_3Ge ,” *Bulletin of the American Physical Society* (2021).
- [25] Deshun Hong and Anand Bhattacharya, Private Communication (2020).
- [26] Y. Chen, J. Gaudet, S. Dasgupta, G. G. Marcus, J. Lin, T. Chen, T. Tomita, M. Ikhlas, Y. Zhao, W. C. Chen, M. B. Stone, O. Tchernyshyov, S. Nakatsuji, and C. Broholm, “Antichiral spin order, its soft modes, and their hybridization with phonons in the topological semimetal Mn_3Ge ,” *Phys. Rev. B* **102**, 054403 (2020).
- [27] K. Momma and F. Izumi, “Vesta 3 for three-dimensional visualization of crystal, volumetric and morphology data,” *J. Appl. Crystallogr.* **44**, 1272 (2011).
- [28] R. F. L. Evans, W. J. Fan, P. Chureemart, T. A. Ostler, M. O. A. Ellis, and R. W. Chantrell, “Atomistic spin model simulations of magnetic nanomaterials,” *J. Phys. Condens. Matter* **26**, 103202 (2014).
- [29] J. L. García-Palacios and F. J. Lázaro, “Langevin-dynamics study of the dynamical properties of small magnetic particles,” *Phys. Rev. B* **58**, 14937 (1998).
- [30] J. W. Cable, N. Wakabayashi, and P. Radhakrishna, “Magnetic excitations in the triangular antiferromagnets mn_3sn and mn_3ge ,” *Phys. Rev. B* **48**, 6159–6166 (1993).
- [31] J. Kübler and C. Felser, “Weyl fermions in antiferromagnetic Mn_3Sn and Mn_3Ge ,” *EPL* **120**, 47002 (2017).
- [32] T. McGuire and R. L. Potter, “Anisotropic magnetoresistance in ferromagnetic 3d alloys,” *IEEE Transactions on Magnetics* **11**, 1018–1038 (1975).
- [33] S. Nandy, G. Sharma, A. Taraphder, and S. Tewari, “Chiral anomaly as the origin of the planar hall effect in weyl semimetals,” *Phys. Rev. Lett.* **119**, 176804 (2017).
- [34] A. A. Burkov, “Giant planar hall effect in topological metals,” *Phys. Rev. B* **96**, 041110(R) (2017).
- [35] D. Ma, H. Jiang, H. Liu, and X. C. Xie, “Planar hall effect in tilted weyl semimetals,” *Phys. Rev. B* **99**, 115121 (2019).
- [36] M. Kimata, N. Sasabe, K. Kurita, Y. Yamasaki, C. Tabata, Y. Yokoyama, Y. Kotani, M. Ikhlas, T. Tomita, K. Amemiya, H. Nojiri, S. Nakatsuji, T. Koretsune, H. Nakao, T. Arima, and T. Nakamura, “X-ray study of ferroic octupole order producing anomalous hall effect,” *Nat. Commun.* **12**, 5582 (2021).
- [37] R. Hartman, “Temperature dependence of the low-field

- galvanomagnetic coefficients of bismuth,” *Phys. Rev.* **181**, 1070 (1969).
- [38] A. Collaudin, B. Fauqué, Y. Fuseya, W. Kang, and K. Behnia, “Angle dependence of the orbital magnetoresistance in bismuth,” *Phys. Rev. X* **5**, 021022 (2015).
- [39] Z. Zhu, B. Fauqué, K. Behnia, and Y. Fuseya, “Magnetoresistance and valley degree of freedom in bulk bismuth,” *J. Phys. Condens. Matter* **30**, 313001 (2018).